Journal of Materials Chemistry A

ROYAL SOCIETY OF CHEMISTRY

PAPER

View Article Online
View Journal | View Issue

Cite this: J. Mater. Chem. A, 2021, 9, 19922

Phase modulation of 1T/2H $MoSe_2$ nanoflowers for highly efficient bifunctional electrocatalysis in rechargeable Li–O_2 batteries†

Qing Xia,‡[a] Lanling Zhao, ‡[b] Deyuan Li,[a] Jun Wang, *[ac] Lili Liu,[d] Chuanxin Hou,[e] Xiaomeng Liu,[a] Haoran Xu,[a] Feng Dang[a] and Jintao Zhang [c]

Received 29th April 2021
Accepted 14th June 2021

DOI: 10.1039/d1ta03584c

rsc.li/materials-a

Li–O_2 batteries with outstanding energy density are considered to be promising next-generation power sources for various future electric devices. However, the battery performance is limited by the inferior electrocatalytic activity of catalysts in the cathode. In this work, $MoSe_2$ catalysts with hybrid 1T and 2H phases were prepared through an efficient two-step hydrothermal strategy. The combination of the 1T phase with the 2H phase could synergically enhance the catalytic activities towards both oxygen reduction reaction and oxygen evolution reaction, and the built-in heterojunction between them also dramatically facilitated the interfacial charge transfer kinetics. Additionally, the hierarchical flower-like architecture with multidimensional channels would promote the rapid electron and mass diffusion, as well as provide enough space for storing discharge products. Thanks to the above merits, $MoSe_2$ cathodes delivered improved electrocatalytic properties for Li–O_2 batteries. This present work may pave a new avenue for highly efficient bifunctional electrocatalyst construction for Li–O_2 batteries.

Introduction

Increasing global warming issues and reduction of fossil energy have promoted the development of energy storage and conversion technologies.[1–3] Among them, non-aqueous Li–O_2 batteries (LOBs) based on the oxygen reduction reaction (ORR) and oxygen evolution reaction (OER) have attracted extensive attention because of their ultrahigh energy density (3500 W h kg^{-1}), which is 10 times that of Li-ion batteries.[4–6] Their further development, however, is currently hindered by low electrocatalytic efficiency and poor cycling stability, which are associated with sluggish reaction kinetics of insulated and insoluble Li_2O_2 formation and decomposition.[7–9] In response, development of efficient bifunctional cathode catalysts for promoting electrocatalytic reactions of LOBs is urgently needed.

Noble metals have been proven to exhibit high-efficiency catalytic properties in LOBs.[10–12] Unfortunately, because of the expensive and scarce precious metal resources, their large-scale application is restricted, and it is necessary to develop cost-effective efficient catalysts. So far, a variety of earth-rich metals and corresponding compounds have been intensively investigated as alternatives, including alloys,[13,14] transition metal oxides,[15–17] sulfides,[18–20] carbides,[21,22], carbon based materials,[23–25] *etc*. In recent years, it is evident that two-dimensional transition metal chalcogenides (2D-TMCs) could exhibit favorable electrocatalytic activities and hold great promise as cathode catalyst candidates for LOBs.[26–28] Typically, they show a layered X–M–X sandwich structure constructed from the crystal units connected by weak van der Waals forces along the *c*-axis, in which M mainly represents Mo, W or Re, and X can be S, Se or Te. As a member of TMCs, $MoSe_2$ displays tunable structures and low Gibbs free energy ($\Delta G_H \sim 0.05$ eV),[29] and their unique layered architecture could facilitate the insertion and extraction of ions,[30,31] making it widely applied in the energy-related research fields, such as supercapacitors,[32,33] batteries,[34,35] water splitting,[36,37] hydrogen catalysis[38,39] and so on. In fact, $MoSe_2$ appears in the form of 2H and 1T phases according to different arrangement of Se atoms. Notably, the 2H phase (triangular prism structure) shows semiconductor characteristics with a band gap between 1.3 and 1.9 eV, and the exposed edge sites were proved to endow it with remarkable

[a]Key Laboratory for Liquid-Solid Structural Evolution and Processing of Materials (Ministry of Education), Shandong University, Jinan 250061, China. E-mail: jw707@sdu.edu.cn

[b]School of Physics, Shandong University, Jinan, 250100, P. R. China

[c]Key Laboratory for Colloid and Interface Chemistry (Ministry of Education), School of Chemistry and Chemical Engineering, Shandong University, Jinan 250061, China

[d]School of Energy Science and Engineering, Institute for Advanced Materials, Nanjing Tech University, Nanjing 211816, Jiangsu Province, China

[e]School of Environmental and Material Engineering, Yantai University, No. 30 Qingquan Road, Yantai, Shandong, 264005, China

† Electronic supplementary information (ESI) available: SEM images and BET results of MS, MS-5, MS-15 and MS-20, SAED pattern, HRTEM image and the intensity profile of MS-10, XPS results and rate performance of MS, MS-5, MS-10, MS-15 and MS-20, image of the hermetic container for Li–O_2 batteries, galvanostatic discharge–charge curve of the pure carbon cathode, SAED pattern of the discharged MS-10 cathode, and cycling performance of KB, MS, MS-5, MS-15 and MS-20 cathodes. See DOI: 10.1039/d1ta03584c

‡ These authors contributed to this work equally.

eletrocatalytic ability.[40,41] Zhang *et al.*[42] successfully grew 2H $MoSe_2$ nanosheets on the surfaces of hollow carbon nanofibers with rich edge sites exposed, delivering a charge voltage platform of 3.69 V at 0.1 mA cm^{-2} in LOBs. Long's group[43] also synthesized 2H $MoSe_2$ nanosheets as cathode catalysts for LOBs, showing good cycle performance of 86 cycles at 500 mA g^{-1} with a fixed specific capacity of 4000 mA h g^{-1}. However the 1T phase (octahedral structure) could deliver metallic properties with a good electrical conductivity (10^7 times that of the 2H phase), which can accelerate charge injection/transfer and thus lead to advanced electrocatalytic activities.[44,45] To the best of our knowledge, reports on 1T $MoSe_2$ catalysts for LOBs are rare. This is because traditional preparation methods of 1T $MoSe_2$ are complicated and usually accompanied by high risks of using metallic Li,[29] and 1T $MoSe_2$ is also thermodynamically metastable, which can be easily transformed into stable 2H $MoSe_2$ by repacking.[46] In this regard, it is a rewarding strategy to construct a heterostructured $MoSe_2$ catalyst for LOBs, combining the conductive 1T phase with abundant active sites with the environmentally stable 2H phase. In recent years, it is found that 1T phase $MoSe_2$ nanosheets could be prepared by hydrothermal synthesis routes, but excessive strong reducing agent should be involved, such as N_2H_4, $NaBH_4$, making the fabrication process violent and poisonous.[39,46–48] Jiang *et al.*[49] also successfully prepared 1T-$MoSe_2$ nanosheets by a hydrothermal method, but the octylamine solvent used is poisonous and could lead to the coverage of electrocatalytically inactive organic groups on the resulting products. Therefore, there is an urgent need for a green and controllable synthesis method to obtain $MoSe_2$ composites with 1T and 2H phases.

Herein, nanoflower-like 2H $MoSe_2$ nanosheets were prepared by a one-step hydrothermal method, and their 2H phase could be controllably and effectively transformed into 1T and 2H hybrid phases by changing the reaction time of hydrothermal treatment. Benefitting from unique architecture with large surface area and rich heterogeneous interfaces of the hybrid phases, 1T/2H $MoSe_2$ nanoflowers with abundant active sites could promote fast transport of oxygen, ions and electrons to facilitate the ORR and OER during cycling and provide enough space for storing discharge products, and they thus show large specific capacities, low overpotentials, good rate performance and excellent cycle stability.

Experimental

Material synthesis processes

2H $MoSe_2$ nanoflowers were synthesized by a one-step hydrothermal method. Specifically, 0.111 g of SeO_2 and 0.106 g of $Na_2MoO_4 \cdot 2H_2O$ were dissolved in 28 mL deionized water under vigorous stirring. Afterwards, 1 mL $NaBH_4$ aqueous solution (0.1 M) was gradually added into the solution, which was then transferred into a 50 mL Teflon-lined autoclave and kept at 180 °C for 24 hours. A black precipitate was obtained and collected by centrifugation, which was washed four times with alcohol and deionized water. After drying at 60 °C for 12 hours, 2H $MoSe_2$ nanoflowers (MS) were finally obtained. In order to prepare 1T/2H $MoSe_2$ nanoflowers, 60 mg of MS were ultrasonically treated for 20 minutes in 50 mL alcohol and transferred into an 80 mL Teflon-lined autoclave. After keeping at 220 °C for 5, 10, 15 and 20 hours, 1T/2H $MoSe_2$ nanoflowers were yielded, which are denoted as MS-5, MS-10, MS-15 and MS-20, respectively.

Material characterization

The morphology of the samples was observed by using a thermal field emission scanning electron microscope (SEM, Hitachi, S-4800, Japan) and transmission electron microscope (TEM, JEOL, JEM-2100F, Japan) operating at an acceleration voltage of 200 kV. Energy dispersive spectroscopy (EDS) images were collected using an EDS system (Oxford Materials Analysis, UK) equipped on a SEM. The phase investigation was conducted by X-ray diffraction (XRD, Rigaku D/max 2500, Japan) with Cu Kα radiation ($\lambda = 1.54056$ Å) with a scan rate of 2° per minute in the 2θ degree range from 20–80°. X-ray photoelectron spectroscopy (XPS, ESCALAB 250, USA) measurements were carried out to study the surface nature of the elements on the samples. Raman spectroscopy (LabRam HR Evolution, France) was used to study the component of samples. The specific surface area and pore size distribution of samples were measured using a nitrogen adsorption surface area and porosity analyzer (Micromeritics ASAP2020, USA).

Electrochemical measurements

To fabricate cathodes, the as-prepared materials, Ketjen black (KB) and polytetrafluoroethylene (PTFE) were ultrasonically dispersed in an isopropanol solution for 20 minutes according to a mass ratio of 4 : 4 : 2, which were subsequently dropped evenly onto carbon papers and dried in a vacuum oven at 120 °C for 12 hours. Li–O_2 cells for electrochemical measurements were assembled using the prepared cathode, a glass fiber separator, lithium metal foil as the counter anode and an electrolyte of 1 M LiTFSI in TEGDME. They were galvanostatically discharged and charged in a hermetic container filled with high-purity oxygen using a Land battery tester. The specific capacities and currents were calculated based on the weight of the active catalysts supported on the cathodes. A CHI 660E electrochemical workstation was employed to record cyclic voltammograms (CV) at a scan rate of 0.15 mV s^{-1} in the voltage range of 2.35–4.50 V (*vs.* Li^+/Li) and perform electrochemical impedance spectroscopy (EIS) with a sine wave of 10 mV and a frequency range of 100–0.01 Hz. The evolution rate profiles of different gas species were measured by *in situ* differential electrochemical mass spectrometry (DEMS).

Results and discussion

The synthesis diagram of 1T/2H $MoSe_2$ samples is shown in Fig. 1. In the first step, Na_2MoO_4 and SeO_2 powders were ultrasonically dispersed and mixed in deionized water under magnetic stirring, into which a certain amount of $NaBH_4$ aqueous solution was added, and the MS sample was achieved after a hydrothermal treatment. In the second step, the

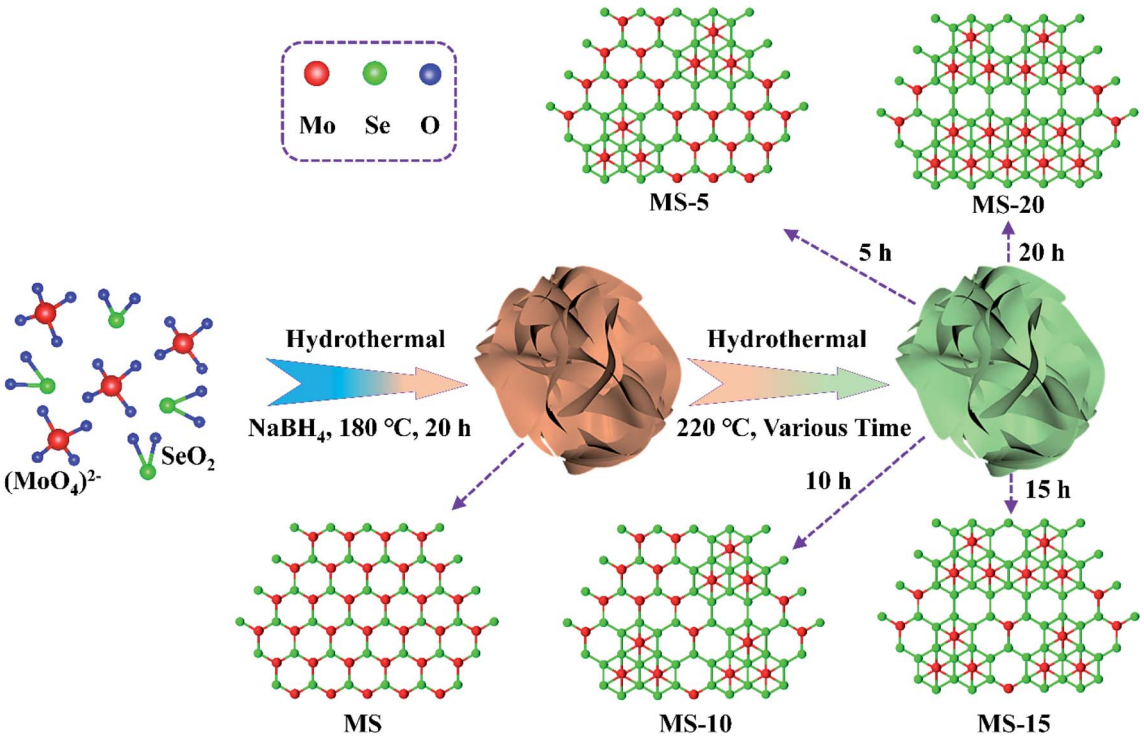

Fig. 1 Schematic illustration of the preparation process of 1T/2H $MoSe_2$ nanoflowers.

obtained product was subjected to another hydrothermal treatment for various reaction times, and $MoSe_2$ samples with different compositions were obtained. 2H $MoSe_2$ phase configuration tends to be energetically more stable than its 1T counterpart, and it is evident that sufficient thermal activation energy introduction could effectively result in phase transition from 2H to 1T.[50,51] In this work, post hydrothermal treatment for the as-prepared 2H $MoSe_2$ offered the driving force to promote this phase transition with atomic replacement, during which Mo atoms partially converted from the state of the prismatic coordination to the antiprismatic coordination,[52,53] evidenced by the following TEM, Raman and XPS results.

SEM images of MS-10 (Fig. 2a) and MS, MS-5, MS-15 and MS-20 (Fig. S1†) show a flower-like structure with sizes of 1–2 μm. The TEM image in Fig. 2c indicates that this structure is actually composed of nanosheets with a thickness of about 50 nm (Fig. 2b). The elemental mapping image and EDS analysis show the uniform distribution of Mo and Se elements, as displayed in Fig. 2g and h. Its crystal structure was characterized by selective area electron diffraction (SAED). As shown in Fig. S2,† the diffraction rings with the radii of 0.283, 0.240, 0.192, 0.169, 0.144, 0.110 and 0.105 nm correspond to the (100), (103), (105), (110), (200), (1011) and (213) planes of the hexagonal $MoSe_2$, respectively. Compared with the standard 2H $MoSe_2$ crystal plane spacing, the slightly larger crystal plane spacings of (103), (105) and (110) for MS-10 indicate that MS-10 may be closely related to the introduction of 1T phase $MoSe_2$. To confirm this conclusion, the high-resolution transmission electron microscope (HRTEM) image of MS-10 was recorded and shown in Fig. S3.† It can be clearly seen that the interplanar distance in the yellow rectangle is 0.316 nm, which is indexed to (100) planes of 2H $MoSe_2$. The lattice spacing in the red rectangle is 0.739 nm, larger than the maximum interplanar spacing of 2H $MoSe_2$ ((002), 0.646 nm), which is considered to be corresponding to the (002) crystal plane of 1T $MoSe_2$ in previous reports.[29,46] It is worth noting that there are two different atomic arrangements in Fig. 2d, which are associated with the 1T and the 2H phases, respectively, and Fig. 2e and f are enlarged HRTEM images of Fig. 2d. Obviously, the Mo atoms of the 2H phase display trigonal prismatic coordination in Fig. 2e, while the 1T phase shows a different arrangement with an octahedral or trigonal antiprismatic symmetry in Fig. 2f.[53,54] All the above results proved that 2H and 1T phases coexist in MS-10.

In order to study the compositions and phase states of different samples, XRD, Raman and XPS measurements were conducted. As shown in Fig. 3a, the sharp peaks at 31.7, 37.9, 47.5 and 56.1° can be assigned to (100), (103), (105) and (110) faces of $MoSe_2$ (JCPDS no. 29-0914), respectively. This means that there are no other crystalline impurities in the as-prepared $MoSe_2$ samples. Raman spectroscopy is a powerful tool for distinguishing 1T and 2H phases, and the corresponding results are listed in Fig. 3b. There are only two vibration modes at 240 and 288 cm^{-1} in the MS, corresponding to the A_{1g} and E_{2g} phonon modes,[47] respectively. In other samples, there are other strong peaks found at 195 (J_1) and 350 (J_2) cm^{-1}, indicating that the 1T and 2H phases coexist in these samples. This is well consistent with the SAED and HRTEM results. More importantly, it can be clearly seen that as the reaction time extended in the second hydrothermal treatment, the 1T phase ratios in the samples continuously increased, which demonstrates that

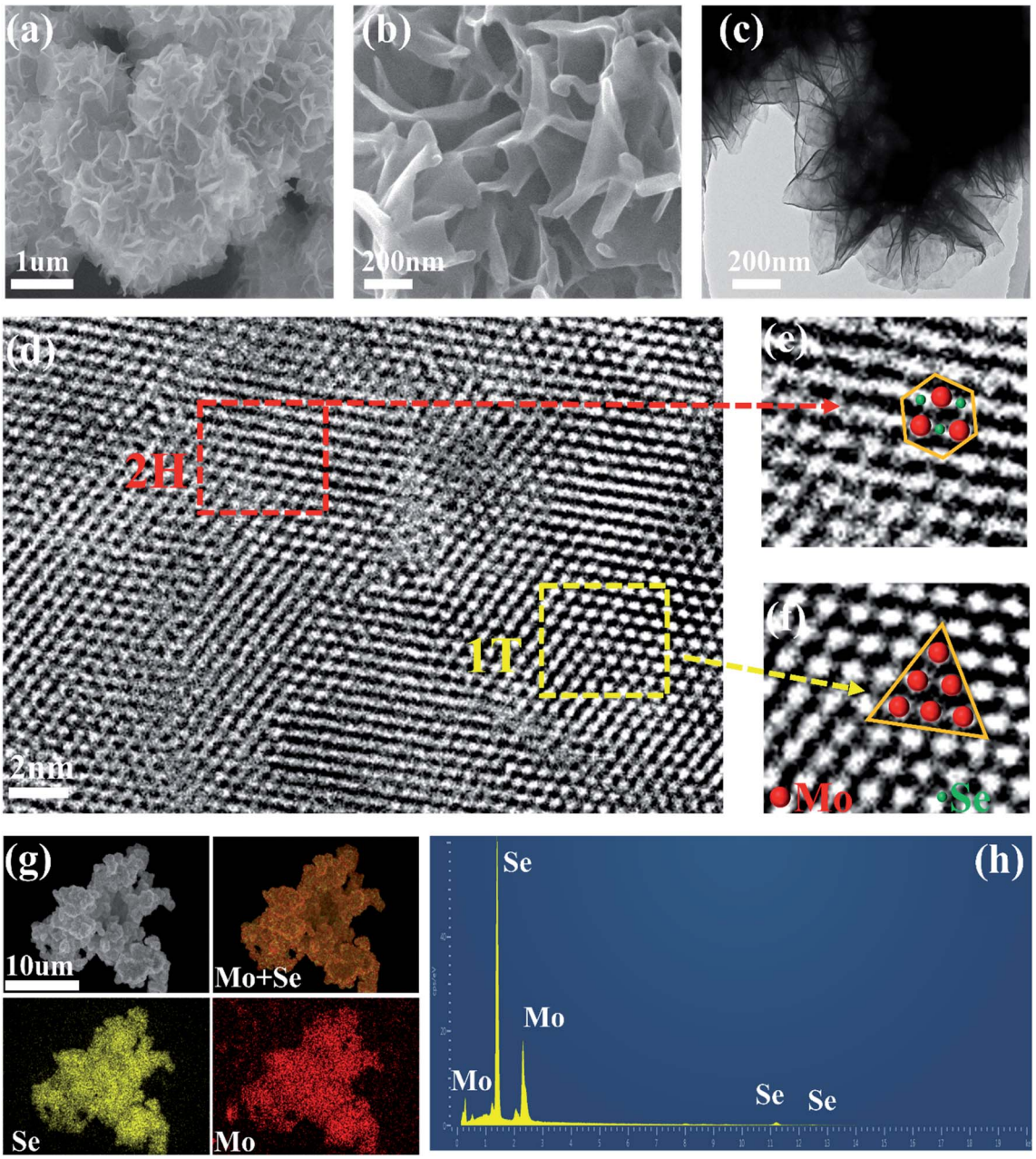

Fig. 2 (a and b) SEM images of MS-10; (c) TEM image of MS-10; (d–f) HRTEM images showing the trigonal prismatic and octahedral unit cell structures, indicating the 2H and 1T phases, respectively; (g) elemental mapping images and (h) EDS analysis of MS-10.

longer reaction time can be helpful for transforming the 2H phase into the 1T phase. Fig. S4† provides the XPS survey spectra of these samples. It is evident that only Mo, Se and C elements were detected on the surfaces of the samples, and the appearance of the C element may be due to the adhesive on the conductive tape. What is more, the ratios of 1T and 2H phases can be further obtained by fitting and analyzing the high-resolution XPS spectra of Mo 3d in Fig. 3d–h. Clearly, there are two characteristic peaks in each spectrum, including the higher energy peak and the lower energy peak, corresponding to Mo $3d_{3/2}$ and Mo $3d_{5/2}$ orbitals, respectively. The higher strength peaks at 228.5 and 231.6 eV were attributed to Mo $3d_{5/2}$ and Mo $3d_{3/2}$ of 1T-$MoSe_2$, and the weaker peaks at 228.9 and 232 eV were related to Mo $3d_{5/2}$ and Mo $3d_{3/2}$ of 2H-$MoSe_2$, respectively. Based on these results, the corresponding 1T and 2H phase contents can be obtained by integrating the areas under the different peaks. As shown in Fig. 3i, it was calculated that the 1T phase ratios of the MS, MS-5, MS-10, MS-15 and MS-20 samples are respectively 1.2, 25.6, 42.3, 59.6 and 81.1%, which implies that with the increase of the reaction time, the proportion of the 1T phase gradually increases, which is in good agreement with the Raman results.

N_2 adsorption–desorption isotherm and pore size distribution analyses were carried out on different $MoSe_2$ samples, and

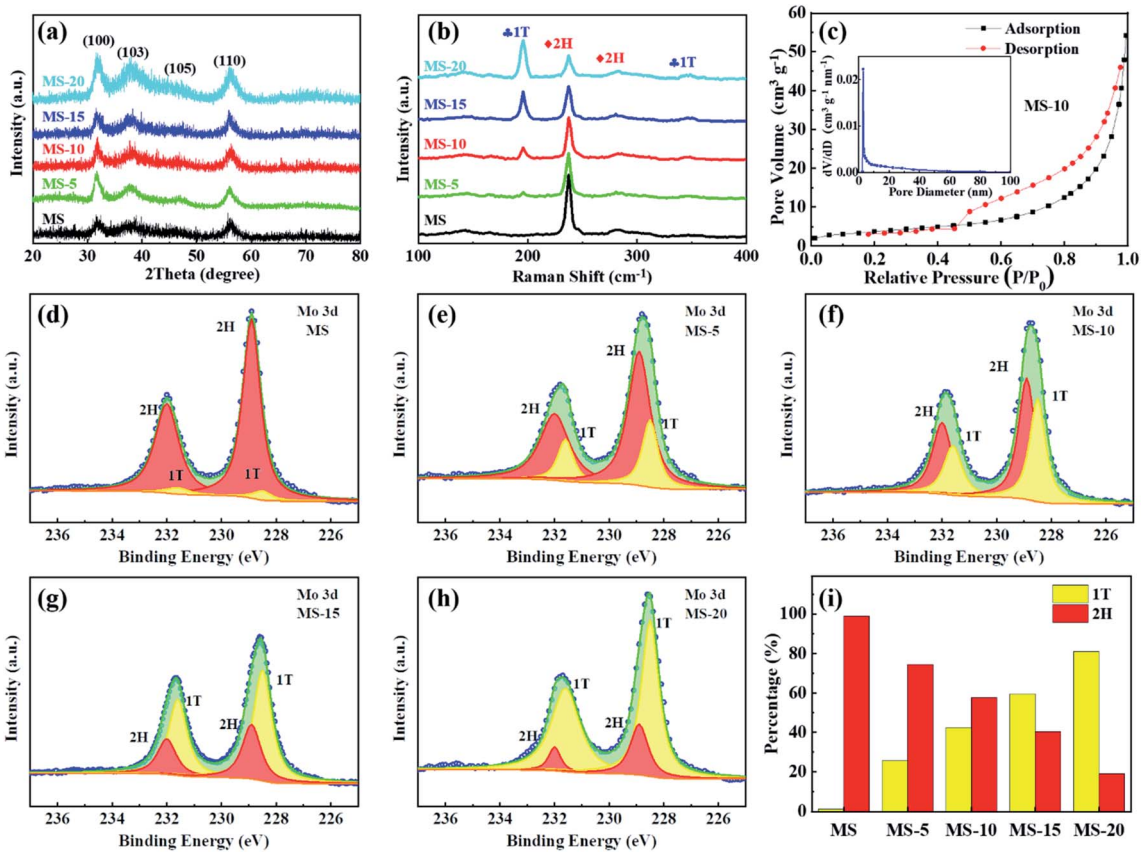

Fig. 3 (a) XRD patterns, (b) Raman spectra, (d–h) high-resolution XPS spectra of Mo 3d and (i) ratios of 1T and 2H phases of different samples; (c) nitrogen adsorption–desorption isotherms with pore size distribution curve of MS-10.

the results are presented in Fig. 3c and S5.† All the N_2 adsorption isotherms of these samples show that the IV type H3 hysteresis loop is in the P/P_0 range of 0.4 to 1.0. Among the observed isotherms, the hysteresis loop exhibits a saturated adsorption platform, indicating the uniform pore formation. It is evident that the BET specific surface areas of different samples are 13.5, 16.4, 16.6, 17.1 and 18.3 $m^2\ g^{-1}$, and the total pore volumes are 0.084, 0.079, 0.082, 0.910 and 0.881 $cm^3\ g^{-1}$, respectively. By analyzing their pore size distributions, it is concluded that the pore sizes of the samples are mainly around 3–20 nm. This demonstrated that for different treatment durations, although the composition of the 1T and 2H phases has changed greatly, the microscopic morphology and pore size distributions are actually similar. It would also ensure that the difference in electrochemical performance of different samples is mainly caused by the difference in phase compositions, but not affected by their microstructures. Electrocatalytic activities of different samples as the cathode catalysts were evaluated in a hermetic container purchased from NJ Scientific Ltd in Fig. S6,† shown in Fig. 4. LOB cells with carbon paper (Fig. S7†) and KB cathodes were also assembled and included to eliminate the influence and confusion caused by their own electrocatalytic properties. Fig. 4a presents the initial discharge/charge curves of different cathodes at 100 mA g^{-1} with a voltage window of 2.35–4.4 V. Compared with the KB counterpart, $MoSe_2$ cathodes show significantly improved coulombic efficiency and discharge/charge specific capacities. Specifically, discharge/charge specific capacities of KB, MS, MS-5, MS-15 and MS-20 cathodes are 3842.2/1301.3, 8088.5/6032.2, 18150.8/17805.6, 15056.2/14941.8 and 12385/10228 mA h g^{-1}, and their coulombic efficiencies are 34%, 75%, 98%, 99% and 82% respectively. In contrast, the MS-10 cathode exhibits the highest discharge/charge specific capacities of 21112.4/20740.7 mA h g^{-1} with the coulombic efficiency of 98%. The reason for the better performance of the $MoSe_2$ cathode was attributed to the unique nanoflower architecture composed of abundant nanosheets, and they expose a large number of active edge sites (Fig. 2a–c), favorable for delivering excellent electrocatalytic activities.[42,54,55] Moreover, it is worth noting that the 1T/2H $MoSe_2$ cathodes show lower charge and discharge overpotentials than those of the MS cathode. This is closely related to the high ORR/OER bifunctional electrocatalytic activity of the 1T phase, and the abundant heterojunctions formed by the two phases will also accelerate the electron transport and promote the reaction kinetics. In addition, MS-5 and MS-10 cathodes deliver obvious two voltage platforms at around 3.5 and 4.2 V during charging, which are considered to be related to the decomposition of the Li-deficient solid solution ($Li_{2-x}O_2$) phase and the oxidation of Li_2O_2, respectively.[56] In order to further illustrate the ORR/OER electrocatalytic performance of different

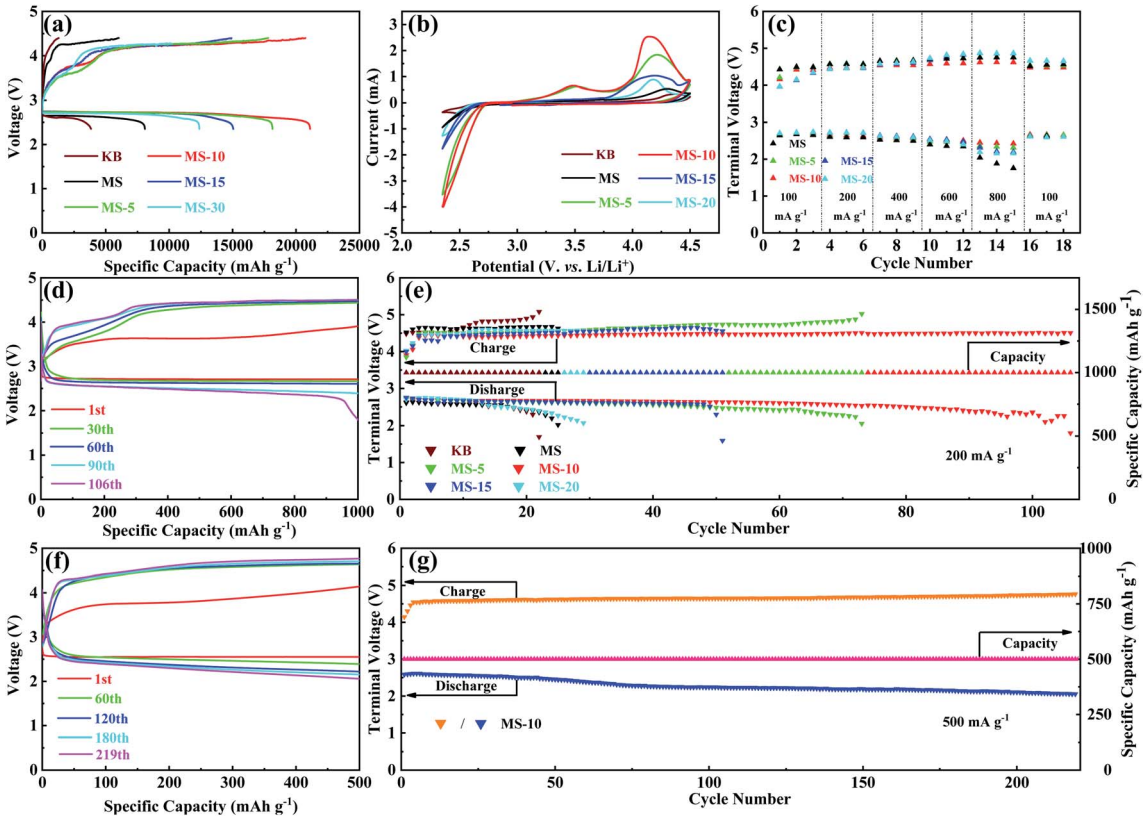

Fig. 4 (a) Initial discharge/charge profiles of different cathodes at 100 mA g^{-1} from 2.35–4.4 V; (b) CV curves of different cathodes at 0.15 mV s^{-1}; (c) comparison of rate performance of different cathodes; (d) typical discharge/charge profiles of the MS-10 cathode at 200 mA g^{-1} under a specific capacity limit of 1000 mA h g^{-1}; (e) cycling performance of different cathodes at 200 mA g^{-1}; (f) typical discharge/charge profiles of the MS-10 cathode at 500 mA g^{-1} under a specific capacity limit of 500 mA h g^{-1}; (g) cycling performance of the MS-10 cathode at 500 mA g^{-1}.

cathodes, CV tests were performed in the range of 2.35–4.5 V, and the results are given in Fig. 4b. It is clearly revealed that the MS-10 cathode displays lower OER potentials and higher ORR potentials, and it also delivers much higher peak current densities than those of other cathodes. More importantly, obvious OER peaks appeared at around 3.5 V for MS-5 and MS-10 cathodes, which have not been detected in the CV plots of other cathodes, and the reason can be clarified by XPS analysis in Fig. S8† for different cathodes charged to 3.5 V at 100 mA g^{-1}. Based on high-resolution Li 1s XPS spectra of different cathodes, the discharge products of MS-5 and MS-10 cathodes contain 14 and 18% $Li_{2-x}O_2$, respectively, while those of MS, MS-15 and MS-20 cathodes contain $Li_{2-x}O_2$ less than 5%. The oxidation peaks at around 3.5 V are related to the reaction of $Li_2O_2 \rightarrow Li_{2-x}O_2 + xLi^+ + xe^-$,[18,57] and thus MS-5 and MS-10 cathodes show specific oxidation peaks, which were not observed for other samples. Fig. 4c and S9† show the rate performance of different cathodes at 100–800 mA g^{-1} for each 3 cycles under a specific capacity limit of 1000 mA h g^{-1}. Fig. 4c gives the information on the discharge/charge terminal voltages with the variation of current densities. It was also traced that even when the current density increases from 100 to 800 mA g^{-1}, the discharge and charge terminal voltages of the MS-10 cathode exhibit only a decrease and increase of 0.22 and 0.21 V, respectively, as shown in Fig. S9.† When the current density returned to 100 mA g^{-1}, its discharge/charge terminal voltages are almost unchanged, compared with those at the initial stages with lower overpotentials in Fig. 4c, which is far more stable than other cathode counterparts.

The cycling performance of different cathodes was compared at 200 mA g^{-1} with a cut-off specific capacity of 1000 mA h g^{-1} in Fig. 4d, e and S10.† It is evident that KB, MS and MS-20 cathodes cannot remain stable within 30 cycles. However MS-5, MS-10, and MS-15 cathodes show extended cycling life, and the MS-10 cathode could be even discharged and charged for more than 100 cycles, demonstrating that introducing a certain amount of the 1T phase into the $MoSe_2$ cathode could effectively activate its electrocatalytic activity and improve the cycling stability. What is more, MS-5 shows higher overpotentials than those of MS-15 and MS-20 during cycling, but it cycled more times, benefiting from the excellent stability of the 2H phase. In addition, as shown in Fig. 4f and g, the MS-10 cathode could be circulated stably for 219 cycles at 500 mA g^{-1} with a cut-off specific capacity of 500 mA h g^{-1}, showing a long cycle life at the high current density. In addition, compared with the most of the reported TMC based cathode catalysts (Table S1†), it is worth mentioning that the 1T/2H $MoSe_2$ cathodes deliver better performance than them under similar testing conditions, including specific capacities, coulombic efficiency and cycling stability.

In order to reveal the effect of the heterogeneous interface in the 1T/2H $MoSe_2$ on the LOB performance, EIS measurements were conducted, and mass diffusion rates for different cathodes could be obtained from the Warburg elements (W) at open circuit potentials,[58,59] which were fitted using an equivalent circuit in Fig. S11a.† Specifically, MS-5, MS-10, MS-15 and MS-20 cathodes respectively deliver mass diffusion rates of 2.084×10^{-2}, 2.522×10^{-2}, 2.488×10^{-2} and 2.485×10^{-2} Ω^{-1} cm^{-2} $s^{0.5}$, much higher than that of the MS (1.466×10^{-2} Ω^{-1} cm^{-2} $s^{0.5}$) cathode, as depicted in Fig. S11b.† This indicates that rich heterogeneous interfaces in the 1T/2H $MoSe_2$ cathodes can greatly increase the mass diffusion rates, thus accelerating the ORR/OER kinetics. In addition, the charge transfer resistances are also summarized in Fig. S11c,† and it is found that the charge transfer resistances of MS-5, MS-10, MS-15 and MS-20 cathodes are 30.67, 20.38, 36.70 and 43.41 Ω, which are much smaller than that of the MS cathode (73.23 Ω). This is due to the introduction of the highly metallic 1T phase in the composites, and the rich heterogeneous interfaces between the two phases also contribute to the improvement of their electrical conductivity.

The synergetic effect from 1T and 2H phases played a critical role in increasing the electrocatalytic activities of $MoSe_2$ cathodes. Notably, the 1T phase features high intrinsic catalytic activity, which could largely reduce the overpotentials of the ORR/OER and optimize battery efficiency, while the 2H phase is helpful for maintaining the structural stability of the cathodes during cycling. Besides, it is believed that the *in situ* incorporation of 1T and 2H phases would generate a heterostructure to enable intimate electrocontact between each other, aiding in increasing electrical conductivity and boosting Li^+ diffusion kinetics for LOBs. Additionally, the nanoflower-like structure composed of porous nanosheets provides enough three-phase interfaces and free spaces to facilitate the deposition and storage of discharge products, optimizing the electrocatalytic performance of $MoSe_2$ cathodes.

To further interpret the excellent eletrocatalytic activity and cycling stability of MS-10, the cathodes at various stages were characterized by XRD, SEM and EIS measurements. Compared with the fresh cathode in Fig. 5a, obvious film-like substances appeared on the surface of the MS-10 cathode after 1st discharging in Fig. 5b. At this stage, two peaks could be traced at 32.7 and 34.8° in Fig. 5e, corresponding to the (200) and (201) crystal planes of Li_2O_2 (JCPDS 73-1640), respectively. With discharge and charge processes being repeated for the 1st and 100th cycles, Li_2O_2 is not detected in the cathode (Fig. 5c–e), which implies that the MS-10 cathode can effectively catalyze the formation and decomposition of Li_2O_2 and almost no insoluble by-products were produced during cycling. The EIS plots of the MS-10 cathode at different stages were recorded and shown in Fig. 5f, and the values of each parameter were fitted in Table S2† using the equivalent circuit shown in the inset. R_{ohm} represents ohmic resistance of the Li–O_2 cell. R_{int1} and R_{int2} denote the charge transfer resistance between the cathode/electrolyte and Li anode/electrolyte, respectively. W denotes mass diffusion rate, which is related to the speed of transporting reaction species. R_{int1} increased from 20.38 to 80.24 Ω after 1st discharging, which would be caused by the deposition of insulated Li_2O_2 on the surface of the cathodes. It then obviously decreased to 28.22 Ω after 1st charging, mainly due to the decomposition of Li_2O_2. Notably, the R_{int1} increase of the MS-10 cathode after the 100th cycle is not obvious, indicating its good reversibility. In addition, XPS measurement for the MS-10 cathode after cycling test was conducted, and the result in Fig. S13† indicates that the ratio of 1T and 2H phases shows almost no changes, compared with that of the as-prepared material, which proves the good structural stability of the MS-10 cathode during cycling.

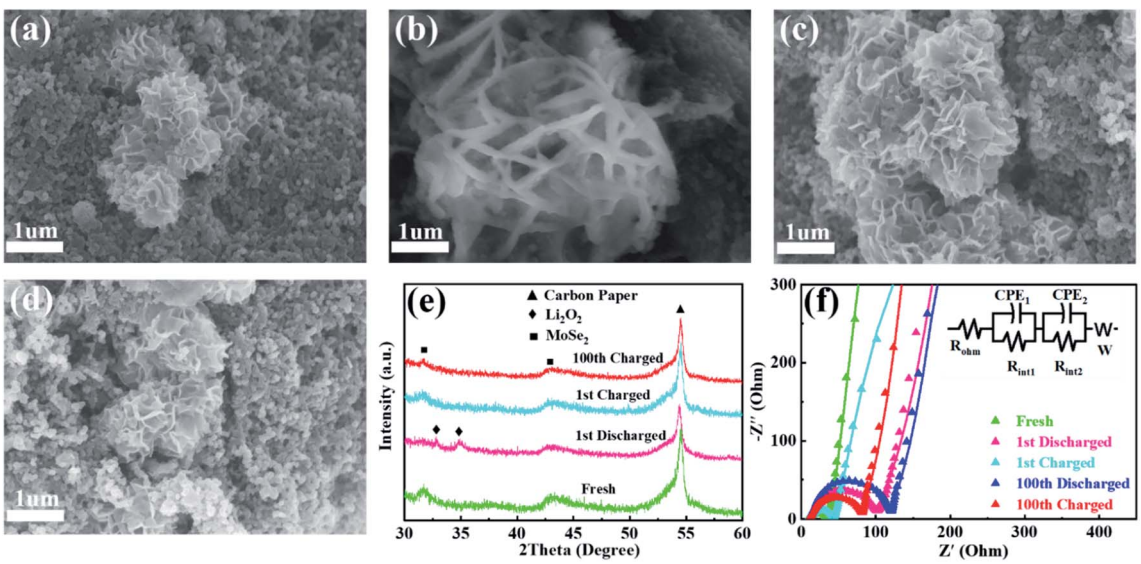

Fig. 5 SEM images of the MS-10 cathodes at different stages: (a) fresh, (b) after 1st discharging, (c) after 1st recharging and (d) after 100th recharging under a limited specific capacity of 1000 mA h g^{-1}; (e) XRD patterns and (f) EIS plots of the MS-10 cathodes at different stages.

Ex situ XPS and SAED of MS-10 cathodes were performed to study the reaction mechanism of MS-10 samples during cycling. Fig. 6b–f show the high-resolution Li 1s XPS spectra at different stages in Fig. 6a. For the pristine cathode, there is no corresponding Li compound peak found in Fig. 6b. When the discharge specific capacity reaches 200 mA h g^{-1} (state I), two peaks can be obtained by fitting the high-resolution XPS spectrum of Li 1 s (Fig. 6c). The peak at 56.1 eV may be related to the $Li_{2-x}O_2$ discharge products, while the other peak at 54.8 eV is caused by the Li_2O_2 deposition on the cathode surfaces.[60,61] When the discharge specific capacity reaches 800 mA h g^{-1} (state II), only one peak of Li_2O_2 can be traced in Fig. 6d, which indicates that $Li_{2-x}O_2$ at state II had been further oxidized to Li_2O_2 totally. This was verified by the corresponding SAED spectrum in Fig. S12† with only diffraction rings of Li_2O_2 and $MoSe_2$, indicating that rare by-products formed at this stage. Based on the above discussion, it can be proposed that the growth mechanism of Li_2O_2 in discharging processes occurred through a typical surface-nucleation route, and the corresponding electrochemical equations are listed as follows:

$$Li^+ + O_{2(SOL)} + e^- \rightarrow LiO_2^* \quad (1)$$

$$Li^+ + LiO_2^* + e^- \rightarrow Li_2O_2^* \quad (2)$$

$$2LiO_2^* \rightarrow Li_2O_2^* + O_2 \quad (3)$$

In addition, when charging to a small amount of specific capacity (100 mA h g^{-1}, state III), the corresponding Li 1s XPS signal can be fitted into two peaks associated with Li_2O_2 and $Li_{2-x}O_2$ (Fig. 6e). Fig. 6g shows the *in situ* DEMS spectrum during the corresponding charging process, which is a typical "M"-shaped curve. According to previous studies, the O_2 release at the beginning of the curve is attributed to decomposition of the non-stoichiometric $Li_{2-x}O_2$ on the cathode with lower overpotentials.[62–64] The corresponding electrochemical equations are given as follows:

$$Li_2O_2 \rightarrow LiO_2 + Li^+ + e^- \quad (4)$$

$$LiO_2 \rightarrow Li^+ + O_2 + e^- \quad (5)$$

At state IV, it can be concluded from Fig. 6f that the product at this stage is almost Li_2O_2, corresponding to the second peak of the DEMS curve, and O_2 in the second mountain escapes from the higher crystallinity Li_2O_2, which could result in a slightly higher overpotential during charging. This means that at a higher voltage of 4.35 V, Li_2O_2 directly turned into Li^+ and

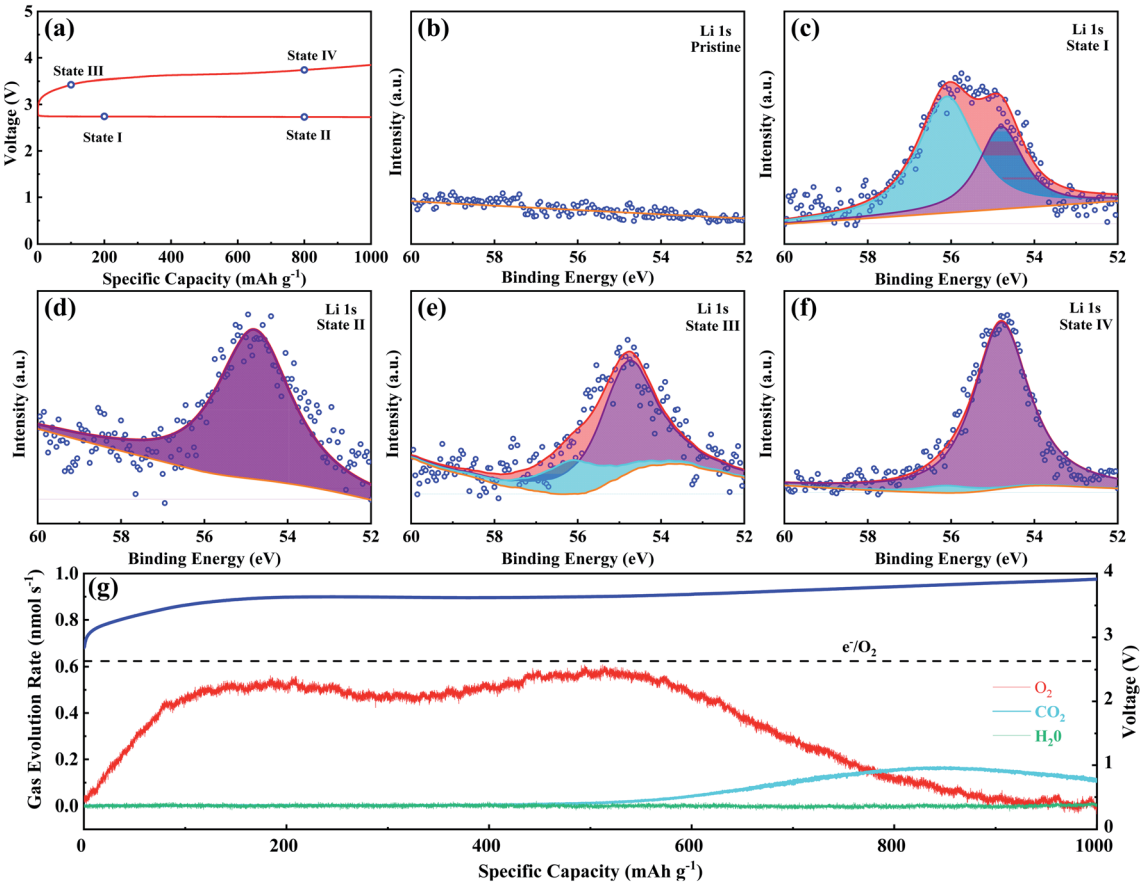

Fig. 6 (a) Discharge and charge curves for the 1st cycle at 200 mA g^{-1} under a cutoff specific capacity of 1000 mA h g^{-1}; (b–f) high-resolution Li 1s XPS spectra at different states of MS-10 cathodes; (g) *in situ* DEMS profiles for the MS-10 cathode with charge curves at 1000 mA g^{-1}.

O_2 through a one-step two-electron transfer process, and the electrochemical equation is given as follows:

$$Li_2O_2 \rightarrow 2Li^+ + O_2 + 2e^- \quad (6)$$

Conclusions

In summary, $MoSe_2$ catalysts with tunable 1T/2H phases were successfully constructed by simply varying the reaction time in the hydrothermal process. Their unique hierarchical framework with large surface area and modified intrinsic structures could not only expose abundant active sites to boost the electron and mass transport, but also provide sufficient storage for discharge products, thus exhibiting superior ORR/OER performance in LOBs. The $MoSe_2$ cathode with 42.3% 1T phase could deliver discharge/charge specific capacities of 21210.4/20740.7 mA h g^{-1} at 100 mA g^{-1}, and it also shows good high rate capability, even at 800 mA g^{-1}. Excellent cyclabilities had been achieved with low polarization, of more than 100 cycles at 200 mA g^{-1} with a fixed capacity of 1000 mA h g^{-1} and 219 cycles at 500 mA g^{-1} with a fixed capacity of 500 mA h g^{-1}. This rational synthetic strategy with effective modulation of hybrid phases and electrocatalytic capability could provide guidance for the application of other TMC materials in LOBs, which is also expected to be extended to various high specific energy storage and conversion systems.

Conflicts of interest

There are no conflicts to declare.

Acknowledgements

Funding support from the China Postdoctoral Science Foundation (2020M672054), Natural Science Foundation of Shandong Province (ZR2020QB122), Young Scholars Program of Shandong University (2019WLJH21), Taishan Scholars Programme of Shandong Province (No. tsqn20161004) and Project for Scientific Research Innovation Team of Young Scholar in Colleges and Universities of Shandong Province (2019KJC025) is gratefully acknowledged.

Notes and references

1 N. Kittner, F. Lill and D. M. Kammen, *Nat. Energy.*, 2017, **2**, 17125.
2 D. Larcher and J. M. Tarascon, *Nat. Chem.*, 2015, **7**, 19–29.
3 Y. Hou, J. Wang, C. X. Hou, Y. Q. Fan, Y. J. Zhai, H. Y. Li, F. Dang and S. L. Chou, *J. Mater. Chem. A*, 2019, **7**, 6552–6561.
4 Y. Yu, G. Huang, J. Z. Wang, K. Li, J. L. Ma and X. B. Zhang, *Adv. Mater.*, 2020, **32**, 2004157.
5 C. T. Zhao, C. Yu, S. H. Liu, J. Yang, X. M. Fan, H. W. Huang and J. S. Qiu, *Adv. Funct. Mater.*, 2015, **25**, 6913–6920.
6 C. X. Hou, W. Yang, X. Xie, X. Sun, J. Wang, N. Naik, D. Pan, X. Mai, Z. Guo, F. Dang and W. Du, *J. Colloid Interface Sci.*, 2021, **596**, 396–407.
7 Z. W. Chang, J. J. Xu and X. B. Zhang, *Adv. Energy Mater.*, 2017, **7**, 1700875.
8 Y. J. Kang, S. C. Jung, H. J. Kim, Y. K. Han and S. H. Oh, *Nano Energy*, 2016, **27**, 1–7.
9 Y. Wang and Y. Xia, *Nat. Chem.*, 2013, **5**, 445–447.
10 D. U. Lee, P. Xu, Z. P. Cano, A. G. Kashkooli, M. G. Park and Z. W. Chen, *J. Mater. Chem. A*, 2016, **4**, 7107–7134.
11 B. Liu, Y. L. Sun, L. Y. Liu, J. T. Chen, B. J. Yang, S. Xu and X. B. Yan, *Energy Environ. Sci.*, 2019, **12**, 887–922.
12 A. J. Hu, C. Z. Shu, C. X. Xu, R. X. Liang, J. B. Li, R. X. Zheng, M. L. Li and J. P. Long, *J. Mater. Chem. A*, 2019, **7**, 21605–21633.
13 Y. C. Lu, Z. C. Xu, H. A. Gasteiger, S. Chen, K. Hamad-Schifferli and Y. Shao-Horn, *J. Am. Chem. Soc.*, 2010, **132**, 12170–12171.
14 J. Suntivich, Z. Xu, C. E. Carlton, J. Kim, B. Han, S. W. Lee, N. Bonnet, N. Marzari, L. F. Allard, H. A. Gasteiger, K. Hamad-Schifferli and Y. Shao-Horn, *J. Am. Chem. Soc.*, 2013, **135**, 7985–7991.
15 Q. C. Zhu, S. M. Xu, M. M. Harris, C. Ma, Y. S. Liu, X. Wei, H. S. Xu, Y. X. Zhou, Y. C. Cao, K. X. Wang and J. S. Chen, *Adv. Funct. Mater.*, 2016, **26**, 8514–8520.
16 J. J. Xu, Z. L. Wang, D. Xu, F. Z. Meng and X. B. Zhang, *Energy Environ. Sci.*, 2014, **7**, 2045–2384.
17 H. L. Wang, Y. Yang, Y. Y. Liang, G. Y. Zheng, Y. G. Li, Y. Cui and H. J. Dai, *Energy Environ. Sci.*, 2012, **5**, 7931–7935.
18 Q. S. Huang, F. Dang, H. T. Zhu, L. L. Zhao, B. He, Y. Wang, J. Wang and X. M. Mai, *J. Power Sources*, 2020, **451**, 227738.
19 J. P. Long, Z. Q. Hou, C. Z. Shu, C. Han, W. J. Li, R. Huang and J. Z. Wang, *ACS Appl. Mater. Interfaces*, 2019, **11**, 3834–3842.
20 X. F. Wang, Y. J. Li, X. X. Bi, L. Ma, T. P. Wu, M. Sina, S. Wang, M. H. Zhang, J. Alvarado, B. Y. Lu, A. Banerjee, K. Amine, J. Lu and Y. S. Meng, *Joule*, 2018, **2**, 2381–2392.
21 M. M. Ottakam Thotiyl, S. A. Freunberger, Z. Q. Peng, Y. H. Chen, Z. Liu and P. G. Bruce, *Nat. Mater.*, 2013, **12**, 1050–1056.
22 H. J. Zhang, K. X. Wang, X. Y. Wu, Y. M. Jiang, Y. B. Zhai, C. Wang, X. Wei and J. S. Chen, *Adv. Funct. Mater.*, 2014, **24**, 3399–3404.
23 C. Z. Shu, Y. M. Lin and D. S. Su, *J. Mater. Chem. A*, 2016, **4**, 2128–2136.
24 Y. F. Li, Z. P. Huang, K. Huang, D. Carnahan and Y. C. Xing, *Energy Environ. Sci.*, 2013, **6**, 3339–3345.
25 J. H. Han, X. W. Guo, Y. Ito, P. Liu, D. Hojo, T. Aida, A. Hirata, T. Fujita, T. Adschiri, H. S. Zhou and M. W. Chen, *Adv. Energy Mater.*, 2016, **6**, 1501870.
26 M. Song, H. Tan, X. L. Li, A. L. Y. Tok, P. Liang, D. L. Chao and H. J. Fan, *Small Methods*, 2019, **4**, 1900274.
27 P. P. Zhang, X. Y. Lu, Y. Huang, J. W. Deng, L. Zhang, F. Ding, Z. Q. Su, G. Wei and O. G. Schmidt, *J. Mater. Chem. A*, 2015, **3**, 14562–14566.

28 Z. M. Sun, J. L. He, M. W. Yuan, L. Lin, Z. Zhang, Z. Kang, Q. L. Liao, H. F. Li, G. B. Sun, X. J. Yang, R. Long and Y. Zhang, *Nano Energy*, 2019, **65**, 103996.
29 N. Li, J. J. Wu, Y. T. Lu, Z. J. Zhao, H. C. Zhang, X. T. Li, Y. Z. Zheng and X. Tao, *Appl. Catal., B*, 2018, **238**, 27–37.
30 J. J. Zhang, W. P. Kang, M. Jiang, Y. You, Y. L. Cao, T. W. Ng, D. Y. W. Yu, C. S. Lee and J. Xu, *Nanoscale*, 2017, **9**, 1484–1490.
31 T. Xiang, S. Tao, W. Y. Xu, Q. Fang, C. Q. Wu, D. B. Liu, Y. Zhou, A. Khalil, Z. Muhammad, W. S. Chu, Z. H. Wang, H. F. Xiang, Q. Liu and L. Song, *ACS Nano*, 2017, **11**, 6483–6491.
32 Z. Jiang, Y. Wang, S. G. Yuan, L. Shi, N. Wang, J. Xiong, W. H. Lai, X. Y. Wang, F. Y. Kang, W. Lin, C. P. Wong and C. Yang, *Adv. Funct. Mater.*, 2018, **29**, 1807116.
33 P. Pazhamalai, K. Krishnamoorthy, V. K. Mariappan, S. Sahoo, S. Manoharan and S. J. Kim, *Adv. Mater. Interfaces*, 2018, **5**, 1800055.
34 J. M. Ge, L. Fan, J. Wang, Q. F. Zhang, Z. M. Liu, E. J. Zhang, Q. Liu, X. Z. Yu and B. G. Lu, *Adv. Energy Mater.*, 2018, **8**, 1801477.
35 P. Ge, L. M. Zhang, Y. Yang, W. Sun, Y. H. Hu and X. B. Ji, *Adv. Mater. Interfaces*, 2019, **7**, 1901651.
36 N. K. Oh, C. Kim, J. Lee, O. Kwon, Y. Choi, G. Y. Jung, H. Y. Lim, S. K. Kwak, G. Kim and H. Park, *Nat. Commun.*, 2019, **10**, 1723.
37 N. Li, Y. F. Zhang, M. L. Jia, X. D. Lv, X. T. Li, R. Li, X. Q. Ding, Y. Z. Zheng and X. Tao, *Electrochim. Acta*, 2019, **326**, 134976.
38 L. Najafi, S. Bellani, R. Oropesa-Nuñez, A. Ansaldo, M. Prato, A. E. Del Rio Castillo and F. Bonaccorso, *Adv. Energy Mater.*, 2018, **8**, 1801764.
39 Y. Yin, Y. M. Zhang, T. L. Gao, T. Yao, X. H. Zhang, J. C. Han, X. J. Wang, Z. H. Zhang, P. Xu, P. Zhang, X. Z. Cao, B. Song and S. Jin, *Adv. Mater.*, 2017, **29**, 1700311.
40 C. Xu, S. J. Peng, C. L. Tan, H. X. Ang, H. T. Tan, H. Zhang and Q. Y. Yan, *J. Mater. Chem. A*, 2014, **2**, 5597–5601.
41 H. Tang, K. P. Dou, C. C. Kaun, Q. Kuang and S. H. Yang, *J. Mater. Chem. A*, 2014, **2**, 360–364.
42 Y. Q. Lai, W. Chen, Z. A. Zhang, Y. Q. Gan, X. Yang and J. Li, *RSC Adv.*, 2016, **6**, 19843–19847.
43 M. L. Li, C. Z. Shu, A. J. Hu, J. B. Li, Y. Yan, M. He and J. P. Long, *J. Alloys Compd.*, 2021, **855**, 157484.
44 Y. Y. Feng, T. Zhang, J. H. Zhang, H. Fan, C. He and J. X. Song, *Small*, 2020, **16**, 2002850.
45 Y. F. Yu, G. H. Nam, Q. Y. He, X. J. Wu, K. Zhang, Z. Z. Yang, J. Z. Chen, Q. L. Ma, M. T. Zhao, Z. Q. Liu, F. R. Ran, X. Z. Wang, H. Li, X. Huang, B. Li, Q. H. Xiong, Q. Zhang, Z. Liu, L. Gu, Y. H. Du, W. Huang and H. Zhang, *Nat. Chem.*, 2018, **10**, 638–643.
46 W. P. Xiao, D. Bukhvalov, Z. Y. Zou, L. Zhang, Z. X. Lin and X. F. Yang, *ChemSusChem*, 2019, **12**, 5015–5022.
47 Y. H. Li, Y. Zhang, X. L. Tong, X. L. Wang, L. J. Zhang, X. H. Xia and J. P. Tu, *J. Mater. Chem. A*, 2021, **9**, 1418–1428.
48 J. T. Zhang, Y. L. Chen, M. Liu, K. Du, Y. Zhou, Y. P. Li, Z. J. Wang and J. Zhang, *Nano Res.*, 2018, **11**, 4587–4598.
49 M. Jiang, J. J. Zhang, M. H. Wu, W. J. Jian, H. T. Xue, T. W. Ng, C. S. Lee and J. Xu, *J. Mater. Chem. A*, 2016, **4**, 14949–14953.
50 S. J. Deng, C. Z. Ai, M. Luo, B. Liu, Y. Zhang, Y. Y. Li, S. W. Lin, G. X. Pan, Q. Q. Xiong, Q. Liu, X. L. Wang, X. H. Xia and J. P. Tu, *Small*, 2019, **15**, 1901796.
51 H. Y. Shi, H. Zhang, M. J. Li, Y. Wang and D. Z. Wang, *J. Alloys Compd.*, 2021, **878**, 160381.
52 Z. Z. Wu, R. B. Zhang, H. Fei, R. Q. Liu, D. Z. Wang and X. L. Liu, *Appl. Surf. Sci.*, 2020, **532**, 147372.
53 J. Y. Zhang, T. T. Wang, P. T. Liu, Y. G. Liu, J. Ma and D. Q. Gao, *Electrochim. Acta*, 2016, **217**, 181–186.
54 Y. J. Chung, C. S. Yang, J. T. Lee, G. H. Wu and J. M. Wu, *Adv. Energy Mater.*, 2020, **10**, 2002082.
55 S. J. Deng, C. Z. Ai, M. Luo, B. Liu, Y. Zhang, Y. Y. Li, S. W. Lin, G. X. Pan, Q. Q. Xiong, Q. Liu, X. L. Wang, X. H. Xia and J. P. Tu, *Small*, 2019, **15**, 1901796.
56 W. G. Fan, B. Z. Wang, X. X. Guo, X. Y. Kong and J. J. Liu, *Nano Energy*, 2016, **27**, 577–586.
57 S. Ganapathy, B. D. Adams, G. Stenou, M. S. Anastasaki, K. Goubitz, X. F. Miao, L. F. Nazar and M. Wagemaker, *J. Am. Chem. Soc.*, 2014, **136**, 16335–16344.
58 K. Cheng, D. P. He, T. Peng, H. F. Lv, M. Pan and S. C. Mu, *Electrochim. Acta*, 2014, **132**, 356–363.
59 J. J. Xu, Z. L. Wang, D. Xu, L. L. Zhang and X. B. Zhang, *Nat. Commun.*, 2013, **4**, 2438.
60 G. Y. Li, N. Li, S. T. Peng, B. He, J. Wang, Y. Du, W. B. Zhang, K. Han and F. Dang, *Adv. Energy Mater.*, 2020, **11**, 2002721.
61 J. H. Lin, Y. H. Wang, X. H. Zheng, H. Y. Liang, H. N. Jia, J. L. Qi, J. Cao, J. C. Tu, W. D. Fei and J. C. Feng, *Dalton Trans.*, 2018, **47**, 8771–8778.
62 D. W. Kim, S. M. Ahn, J. W. Kang, J. D. Suk, H. K. Kim and Y. K. Kang, *J. Mater. Chem. A*, 2016, **4**, 6332–6341.
63 D. P. Kundu, R. Black, E. J. Berg and L. F. Nazar, *Energy Environ. Sci.*, 2015, **8**, 1292–1298.
64 Y. Bae, D. H. Ko, S. Lee, H. D. Lim, Y. J. Kim, H. S. Shim, H. Park, Y. Ko, S. K. Park, H. J. Kwon, H. Kim, H. T. Kim, Y. S. Min, D. M. Im and K. Kang, *Adv. Energy Mater.*, 2018, **8**, 1702661.